Plasma Science and Technology

PAPER

Plasma diagnostics by optical emission spectroscopy on manganese ore in conjunction with XRD, XRF and SEM-EDS

Plasma Sci. Technol. **21** (2019) 085507 (8pp) https://doi.org/10.1088/2058-6272/ab1977

Plasma diagnostics by optical emission spectroscopy on manganese ore in conjunction with XRD, XRF and SEM-EDS

Muhammad FAHAD[1], **Sajad ALI**[2] **and Yaseen IQBAL**[2]

[1] Department of Electrical and Computer Engineering, COMSATS University Islamabad, Abbottabad Campus, University Road, 22060 Abbottabad, Pakistan
[2] Materials Research Laboratory (MRL), Department of Physics, University of Peshawar, 25120 Peshawar, Pakistan

E-mail: drmuhammadfahad@gmail.com

Received 21 January 2019, revised 10 April 2019
Accepted for publication 15 April 2019
Published 18 June 2019

Abstract

Manganese (Mn) is an important industrial mineral. Information about the chemical and phase constitution along with the concentration of impurities presented in Mn ore is compulsory in assessing its suitability for different applications. We performed the qualitative and quantitative analysis of low-grade Mn ore (LGMO) using laser-induced breakdown spectroscopy (LIBS) in conjunction with x-ray diffraction (XRD), x-ray fluorescence (XRF) and scanning electron microscopy (SEM) coupled with energy dispersive x-ray electron spectroscopy (EDS). The optical emission spectra of the LGMO sample displayed the presence of Mn, Si, Ca, Fe, Al, Mg, V, Ti, Sr, Ni, Na, Ba and Li. The plasma parameters, electron temperature and number density were estimated using the Boltzmann plot and Stark broadening line profile methods and were found to be 7500 K $\pm$ 750 K and 8.18 $\pm$ 0.8 $\times$ 10^{17} cm^{-3}, respectively. Quantitative analysis was performed using the calibration-free LIBS (CF-LIBS) method and its outcome along with XRD, XRF and SEM-EDS data showed almost analogous elemental composition, while the LIBS method gave acceptably precise elemental analysis by detecting the low atomic number element Li besides V and Sr. The results obtained using LIBS for the LGMO exhibited its ability as a powerful analytical tool and XRF, XRD and SEM-EDS as complementary methods for the compositional analysis of complex low-grade mineral ore.

Keywords: plasma diagnostic, optical emission spectroscopy, spectrochemical analysis, laser-induced breakdown spectroscopy, SEM-EDS

(Some figures may appear in colour only in the online journal)

1. Introduction

Manganese (Mn) is a silvery white, hard, brittle allotropic metal. It is one of the twelve most abundant elements making up the Earth's crust. It is often found in combination with other minerals and not as a free element in nature; for example, iron minerals are almost always present in Mn ores. Mn is an important mineral with many industrial applications, the foremost of which is its use in steel production. The steel industry consumes about 92% of the worldwide Mn production. The other important applications of Mn include: the production of dry-cell batteries, non-ferrous alloys, dietary additives, fertilizers, animal feed and chemicals [1–3]. The Mn content in Mn ore is the parameter used to classify it as high, medium or low grade, and to determine its suitability for its use for different purposes [4]. Low-grade Mn ore (LGMO) can be siliceous, ferruginous and aluminous. The exploitation of LGMO, such as silicate- and carbonate Mn ore is on the rise due to the growing market demand for Mn ore products. Many studies have been performed on the chemical and mineralogical characterization of low-grade Mn of different origins and its extraction from relevant ores [5–8]. There are

different established methods for the processing and upgradation of Mn ore. Among these, hydrometallurgy has more advantages than the others, and hence is the most adoptive one. This method includes leaching, separation from gangue elements and primer element refinement [9–17].

Laser-induced breakdown spectroscopy (LIBS) is an atomic emission spectroscopy technique, which uses a focused laser beam to ablate a sample surface. The sample in this case can be in solid, liquid or gaseous state. The laser interaction with the sample creates a high-temperature and high-density plasma, which expands normally to the sample surface. Initially, the hot plasma emits a bremsstrahlung continuum emission. As soon as the plasma cools down, it starts emitting characteristic atomic line spectra of the constituent elements of the sample [18, 19]. The last decade has seen extensive use of the LIBS technique in a wide range of fields [20–29]. The LIBS technique has attracted increasing research attention due to its capability to make real-time measurements, fast and multi-elemental analysis, intrinsic simplicity, non-destructiveness, portability, versatility in comparison to other analytical methods and almost no need for sample preparation. Consequently, the LIBS technique has been used in the qualitative as well as quantitative analyses of samples of geological nature [30–38].

Minerals collected from different locations and depths of mines are known to have diverse chemical and mineralogical compositions with varying characteristics and complexities. To access the importance of naturally occurring solid materials for the desired applications, their elemental composition and mineralogical classification are equally important. The impurities presented in Mn ores can be detrimental for their use in different applications, and these facts demand an in-depth understanding of the mineralogy and chemical composition of the ores. In the present study, to the best of our knowledge, for the first time we applied the LIBS technique for the qualitative and quantitative analysis of complex (having a number of phases) LGMO. The other analytical techniques of x-ray diffraction (XRD), x-ray fluorescence (XRF) and scanning electron microscopy (SEM) equipped with energy dispersive x-ray spectroscopy (EDS) were also used to cross validate and improve the LIBS results. Although the standard analytical techniques of XRD, XRF and SEM-EDS have been used by many researchers for the compositional analysis of Mn ores, these methods are either destructive, time consuming and/or require special attention to the sample preparation. On the other hand, the LIBS technique versatility, as discussed above, in comparison to these standard analytical methods makes it a suitable tool for the compositional analysis. This study, therefore, contributes assessment of the suitability of the LIBS technique in precise and accurate elemental analysis of ore samples comprised of complex minerals; for example, in comparison to other methods.

2. Experimental methodology

For the present study, an LGMO sample was obtained directly from a fresh quarry. The sample was crushed and milled using a pestle and mortar system and then sieved to get equal and

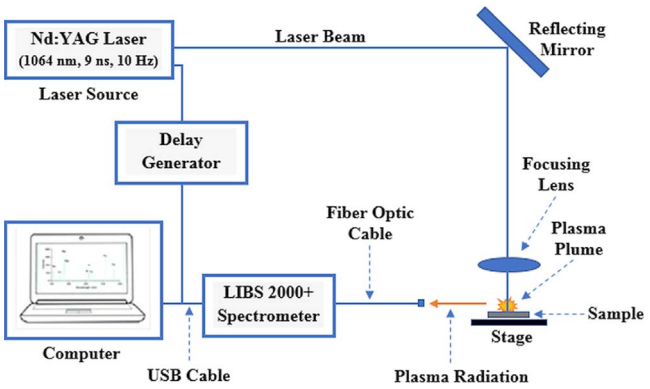

Figure 1. A schematic diagram of the LIBS setup used in the present study.

smooth distribution of constituent particles. One portion of the powder sample was used for the phase analysis via XRD and chemical analysis via XRF, while the other portion was pressed into pellets (3–4 mm in thickness and 13 mm in diameter) for LIBS measurement. A stainless-steel die was used in a manual processing machine to press pellets at ∼30 MPa pressure for 15 min.

The experimental LIBS setup (shown in figure 1) used for the elemental analysis of LGMO in the present study has been discussed in detail in our previous work [39–41]. For qualitative elemental composition determination, the Mn ore sample was ablated using a high power Q-switched Nd:YAG laser. The optical emission spectra of the laser-produced plasma on the sample surface were obtained by focusing a laser beam at the fundamental harmonic (1064 nm) with a repetition rate of 10 Hz and 9 ns pulse duration. At 1064 nm, the in-house laser system is capable of delivering 500 mJ of energy. An energy meter was used for the measurement of laser pulse energy, and we varied the energy by changing the Q-switch delay (OOLIBS software). The energy was optimized at 126 mJ and used throughout the experiment. The Mn ore pellet sample was placed in air under the atmospheric pressure, and the incoming laser beam was focused onto the sample surface using a quartz convex lens (focal length = 20 cm). A set of five spectrometers (LIBS 2000 + spectrometer, Ocean Optics, US) was used to cover a 200–720 nm wavelength range. Each spectrometer had a width of 5 μm in the detection system with a 0.06 nm resolution. An optical emission spectrum of an average of ten data of a single laser shot was used in the present study to analyze the Mn ore sample, and the National Institute of Standards and Technology (NIST) database was utilized for identification purposes [42].

Initially, the identification of crystalline constituent phase(s) of the Mn ore sample and determination of the crystal structure of the constituent phases were carried out using an X'Pert^3 Powder (PANalytical) XRD machine operated at a generator voltage of 45 kV and a current of 40 mA with Cu Kα radiations ($\lambda = 1.54$ Å). The samples were scanned $2\theta = 10°$–$70°$ range in powder form with a count time of 1.0 s/step and 0.03° step size. The comparison of the acquired XRD scan was made with the standard powder diffraction data files (PDF) to identify

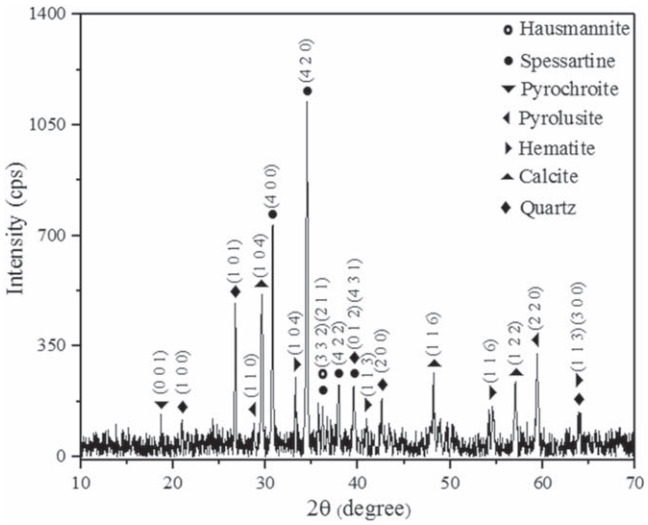

Figure 2. The XRD pattern of the investigated LGMO sample showing the observed peaks and their *hkl* indices.

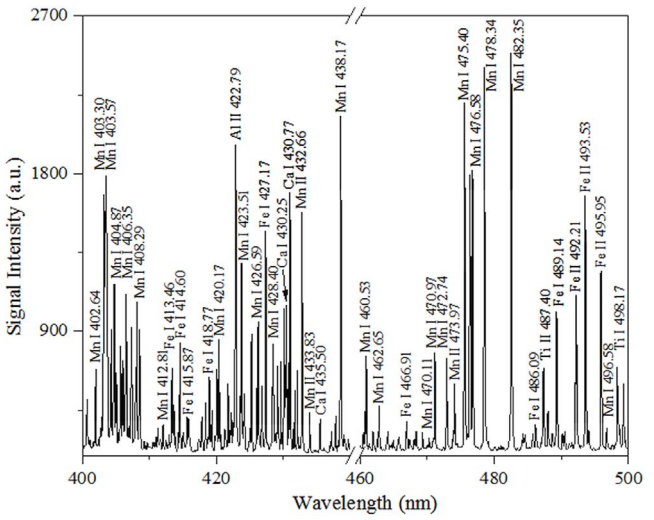

Figure 3. The emission spectrum of the Mn ore sample recorded at the fundamental harmonic showing the 400–440 nm and 460–500 nm wavelength spectral region.

different phases. In the characterization of minerals, high background spiky XRD patterns are common, which exhibit a high degree of overlapping of XRD peaks, and hence, complexity. Background corrections were made to remove the background noise from the obtained XRD spectrum using the PANalytical X'Pert HighScore software. XRF allows relatively rapid, accurate and inexpensive quantitative measurement of the chemical composition of minerals and inorganic materials. For the analysis of surface morphology, and to acquire the semi-quantitative composition data using EDS, a JEOL JSM 5910 SEM-EDS (INCA 200 EDS, Oxford instruments, UK) and a Shimadzu EDS-7000 bench top spectrometer (Shimadzu Co., Kyoto, Japan) were utilized. The spectrometer was equipped with a rhodium (Rh) tube (50 kV) and a silicon drift detector.

3. Results and discussion

The LGMO is a complex mineral in the sense that a number of phases may occur, which makes its accurate phase analysis challenging. At the first stage, the Mn ore in a powder form is subjected to the XRD phase analysis for the assertion of different constituent phases present in it. As shown in figure 2, XRD phase analysis showed the presence of spessartine ($Mn_3Al_2(SiO_4)_3$), pyrolusite (MnO_2), hausmannite (Mn_3O_4), quartz (SiO_2), pyrochroite ($Mn(OH)_2$), hematite (α-Fe_2O_3) and calcite ($CaCO_3$).

3.1. Optical emission spectrum analysis

An optical emission spectrum obtained from a sample usually consists of the spectral lines of the constituent elements, and analysis of these spectral lines can provide information about these components. A representative optical emission spectrum recorded from the LGMO sample in the present study is shown in figure 3. For better resolution, the spectrum has been divided into two wavelength regions of interest: 400–440 nm and 460–500 nm. The presence of dominant lines for Mn, Si, Ca, Fe and Al was observed from the spectrum obtained. A small number of low intensity spectral lines were also observed, showing the presence of Mg, V, Ti, Sr, Ni, Na, Ba and Li. The neutral and singly ionized spectral lines of Fe, Mn and Si were found to dominate the shorter wavelength region.

The most prominent Si (I) line at 288.15 nm corresponding to the transition from $3p4s\,^1P^0_1 \rightarrow 3s^23p^2\,^1D_2$ was also observed in the shorter wavelength region. Most of the neutral and singly ionized Mn lines were detected in the 300–500 nm spectral region. Some of the prominent transitions observed for the neutral Mn in this wavelength region were identified as: $3d^64p^6\,P^0_{3/2} \rightarrow 3d^64s^6D_{3/2}$ at 361.03 nm, $4s4p^4I^0_{11/2} \rightarrow 3d^64s^4H_{9/2}$ at 371.89 nm, $3d^64p^6F^0_{7/2} \rightarrow 3d^64s^6D_{5/2}$ at 383.43 nm, $4s4p^6\,P^0_{3/2} \rightarrow 3d^54s^{26}S_{5/2}$ at 403.44 nm, $4s4d^6D_{9/2} \rightarrow 4s4p^6P^0_{7/2}$ at 446.20 nm, $4s5s^8S_{7/2} \rightarrow 4s4p^8P^0_{5/2}$ at 475.40 nm and $4s5s^8S_{7/2} \rightarrow 4s4p^8P^0_{9/2}$ at 482.35 nm. The neutral lines for Ca at 445.58 nm and Ti at 455.54 nm were observed to have relatively higher intensities due to their higher transition probabilities. Two intense sodium D-lines at 588.99 and 589.59 nm corresponding to the $2p^63p^2P^0_{3/2} \rightarrow 2p^63s^2S_{1/2}$ and $2p^63p^2\,P^0_{1/2} \rightarrow 2p^63s^2S_{1/2}$ transitions, respectively, were also detected. A resonance line of neutral strontium at 460.73 nm corresponding to the $5s5p\,^1P^0_1 \rightarrow 5s^2\,^1S_0$ transition was also observed. Careful analysis of the observed spectra presented traces of Ba and Li as well. These elements were not detected in the XRF, XRD or SEM-EDS analyses due to their limitations for low intensity lines. Some of the observed prominent Mn transitions are shown in figure 4.

3.2. Determination of plasma temperature and electron number density

There are certain prerequisites for characterization of the laser-produced plasma through optical emission spectroscopy. These include optically thin plasma (OTP) and fulfilment of the local thermodynamic equilibrium (LTE) condition [43].

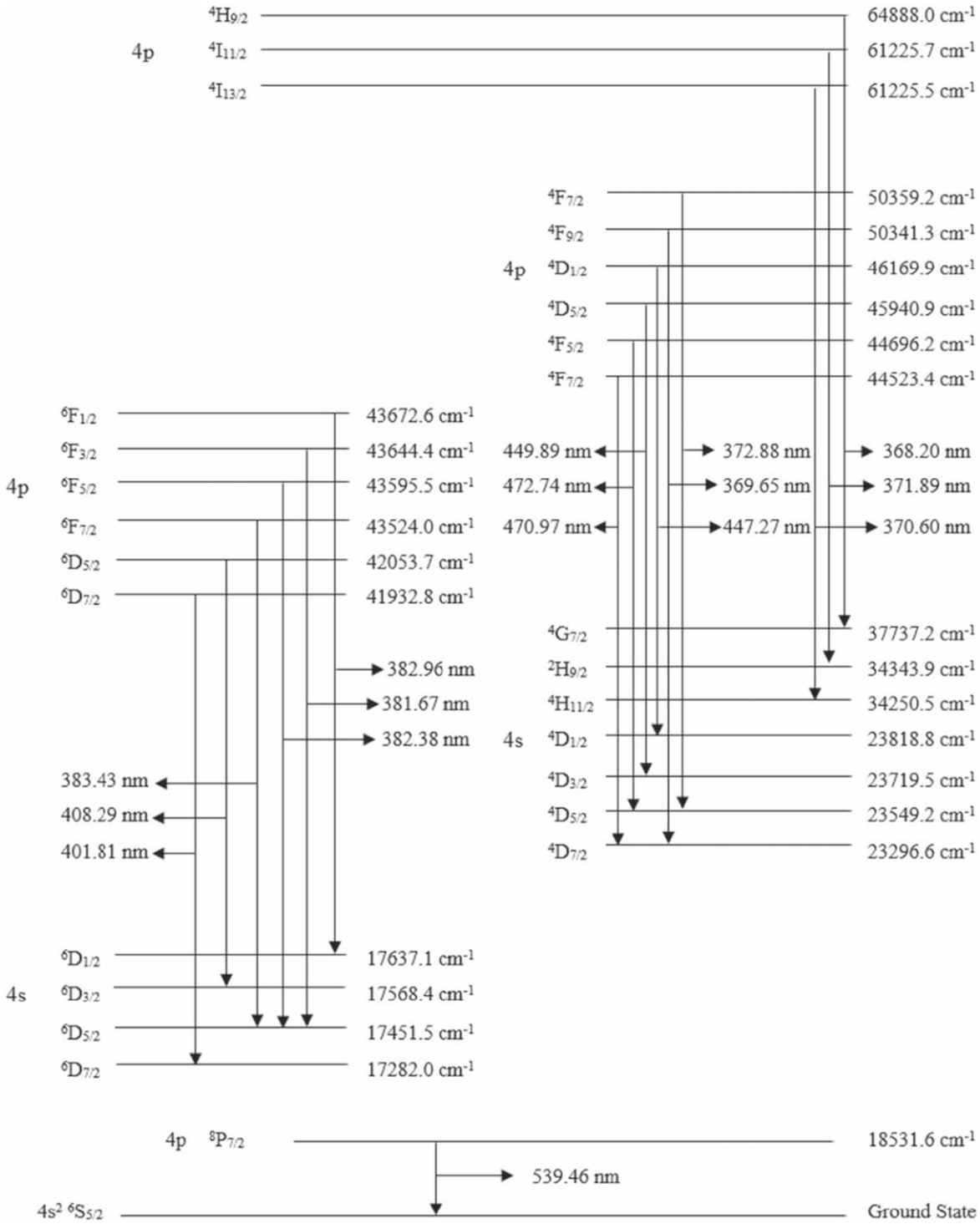

Figure 4. An energy level diagram showing Mn transitions.

The validity of OTP was checked by comparing the experimentally observed intensity ratios with those calculated from the spectroscopic parameters using equation (1):

$$\frac{I_1}{I_2} = \frac{A_1 g_1 \lambda_2}{A_2 g_2 \lambda_1} \exp\left(\frac{-(E_1 - E_2)}{K_B T_e}\right). \quad (1)$$

In equation (1), I_1 and I_2 represent the observed line intensities at wavelengths λ_1 and λ_2 (in nm) along with their corresponding transition probabilities A_1 and A_2, the upper level statistical weights as g_1 and g_2, upper level energies as E_1 (eV) and E_2 (eV), and K_B and T_e are the Boltzmann constant and electron temperature, respectively. The exponential term on the left-hand side of equation (1) can be neglected by selecting two common upper energy levels. In the present study, we made the comparison between Mn (I) spectral lines at 445.30 nm and 447.27 nm ratios with the ratios of their relevant transition probabilities, and the values

Table 1. Spectroscopic parameters of the neutral emission lines of Mn, Ca, Fe and Ti used to construct the Boltzmann plot.

Species	Wavelength λ (nm)	Transition probability A (s^{-1})	Excitation energy E_k (cm^{-1})	g_k
Mn (I)	367.69	7.30×10^7	64 819.53	12
Mn (I)	368.20	7.60×10^7	64 888.00	10
Mn (I)	382.96	1.03×10^7	43 672.66	2
Mn (I)	441.48	2.93×10^7	45 940.93	6
Mn (I)	447.27	4.35×10^7	46 169.93	2
Mn (I)	472.74	1.70×10^7	44 696.29	6
Mn (I)	525.54	4.17×10^6	44 288.74	10
Fe (I)	373.53	2.70×10^7	50 475.28	9
Fe (I)	423.59	1.88×10^7	43 163.32	9
Fe (I)	538.33	7.81×10^7	53 352.98	13
Fe (I)	561.56	2.64×10^7	44 677.00	9
Ca (I)	334.45	1.51×10^7	45 049.07	3
Ca (I)	526.55	4.40×10^7	39 335.32	3
Ca (I)	644.98	9.00×10^6	35 835.41	5
Ti (I)	323.82	2.26×10^7	47 139.73	9
Ti (I)	451.86	6.50×10^6	33 655.86	5
Ti (I)	455.54	1.16×10^7	28 788.38	9

were 1.25 for both of them. Similarly, to cross validate the results, the 250.69/251.61 nm ratio for Si (I) spectral lines and their corresponding transition probability ratios gave 0.326 and 0.325, respectively. The intensity ratios of the selected emission lines from the observed spectra were in good agreement with the calculated ratios from the known spectroscopic parameters for the same lines. The uniformity achieved hence supported our assumption of OTP.

In the present study, the plasma temperature (T_e) was calculated using the Boltzmann plot method. To construct the Boltzmann plot, only those lines were selected which were optically thin and satisfied the other necessary conditions [43, 44]. The lines selected to construct the Boltzmann plot and their corresponding atomic parameters taken from the NIST database [42] are given in table 1.

Using the Mn, Fe, Ca and Ti lines, an average value deduced for the plasma temperature was 7500 K ± 750 K. This apparent plasma temperature (average temperature) can be used to calculate the elemental concentration in the sample. The main source of error in the determination of plasma temperatures comes from the uncertainties in the transition probabilities and in the line intensities measurement. A Boltzmann plot constructed using neutral Mn, Fe, Ca and Ti spectral lines is shown in figure 5. The electron number density (N_e) was determined using the Stark broadening of neutral spectral lines of the constituent elements. The full-width at half maximum (FWHM) of a Stark broadening line is given as [45]:

$$N_e(\mathrm{cm}^{-3}) = \left(\frac{\Delta\lambda_{\mathrm{FWHM}}}{2\omega_s(\lambda, T_e)}\right) \times N_r \qquad (2)$$

In equation (2), $\Delta\lambda_{\mathrm{FWHM}}$ is the Stark contribution to the total line profile, ω_s is the Stark broadening parameter and N_r is the reference electron number density, which is equal to

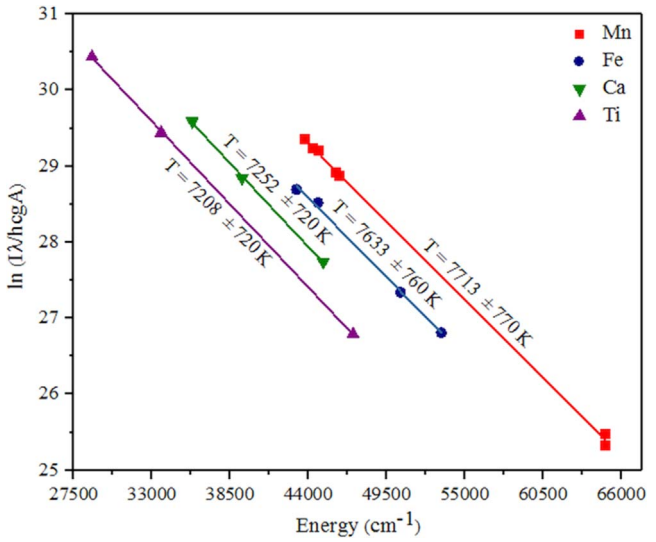

Figure 5. A Boltzmann plot based on selected neutral Mn, Fe, Ca and Ti spectral lines using the fundamental (1064 nm) harmonic of the Nd:YAG laser.

10^{16} (cm^{-3}) for neutral atoms and 10^{17} (cm^{-3}) for the singly charged ions. We used the neutral Si line at 288.15 nm ($3p4s^1P^0_1 \rightarrow 3s^23p^21D_2$) to deduce the N_e, which resulted in $8.18 \pm 0.8 \times 10^{17}\,\mathrm{cm}^{-3}$.

The electron number density calculated using the neutral Ca line at 646.25 nm ($3p^63d4p^3F^0_3 \rightarrow 3p^63d4s^3D_2$) was found to be $1.39 \pm 0.14 \times 10^{17}\,\mathrm{cm}^{-3}$, and was in good agreement with the result obtained using the Si (I) line. In the representative graph for the Si(I) line in figure 6, the dots represent the experimental data points while the continuous line passing through these data points is the Gaussian fit. The lower limit of the electron number density for which the plasma is considered to satisfy the LTE condition is given by the McWhirter criterion as [46]:

$$N_e(\mathrm{cm}^{-3}) \geqslant (1.6 \times 10^{12})T^{1/2}(\Delta E)^3 \qquad (3)$$

where N_e, T (K) and ΔE (eV) represent the electron number density, plasma temperature and upper and lower level energy difference, respectively. The N_e value calculated using equation (3) is about $10^{14}\,\mathrm{cm}^{-3}$, which is much smaller than the calculated value from the Stark-broadened spectral line of Si (I), hence validating the LTE condition.

3.3. Calibration-free LIBS (CF-LIBS) for quantitative analysis

The CF-LIBS technique used in the present study for the quantitative analysis has been discussed in different papers [47, 48]. Accurate determination of electron number density and temperature is an important step in CF-LIBS analysis. The error reported by this method is less than 1%. A simple Boltzmann equation linking the intensities emitted by neutral species in the sample is given as [49]:

$$FC^z = \frac{I_k U^z(T)}{A_k g_k} \exp\left(\frac{E_k}{K_B T}\right). \qquad (4)$$

In this equation C^z represents the neutral atoms' concentration, $U^z(T)$ represents the partition function of the

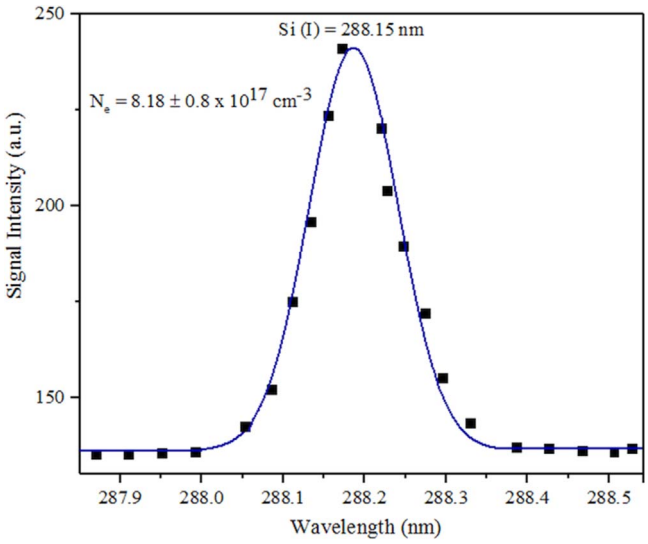

Figure 6. The Stark-broadened profile of the Si (I) spectral line at 288.15 nm wavelength.

emitting element, factor F is related to the mass ablated by the laser from the target surface and can be confirmed by the normalization of the species concentration. Average values of plasma temperature as 0.64 eV and electron number density as $4.78 \pm 0.4 \times 10^{17}\,\mathrm{cm}^{-3}$ were used for the analysis. All the spectroscopic parameters and partition functions for the observed species required for the compositional analysis were taken from the NIST database. Although the above equation (4) can be used to calculate the neutral species (C^z) concentration, for the ionized atoms' (C^{z+1}) concentration, a Saha–Boltzmann equation can be utilized, which relates the two charged states Z and $Z+1$ concentration of any specific element and is given as [50]:

$$n_e \frac{C^{z+1}}{C^z} = \frac{(2m_e kT)^{3/2}}{h^3} \frac{2U_{z+1}}{U_z} \exp\left[-\frac{E_{ion}}{K_B T}\right] (\mathrm{cm}^{-3}). \quad (5)$$

From the above equation, the value for C^{z+1} can easily be deduced while considering the outcomes of equation (4). The total concentration of an element, which is in fact the sum of the neutral and ionic contributions, is thus given as:

$$C^{\alpha}{}_{(T)} = C^{\alpha}{}_{(z)} + C^{\alpha}{}_{(z+1)}. \quad (6)$$

The CF-LIBS method yields the concentration of major elements detected in the LGMO sample as Si (32.8%), followed by Mn, Ca, Fe and Al as 26.5%, 18.9%, 14.0% and 7.8%, respectively.

3.4. Compositional analysis using XRF and SEM-EDS

XRF analysis indicated the presence of major and minor elements in the Mn ore (LGMO sample) as Si (31.96%), followed by Mn, Ca, Fe and Al as 24.17%, 17.80%, 15.12% and 7.19%, respectively. This analysis also showed the presence of other elements, such as Ti, Ni, V, Zn, Sr and Zr, as trace elements (less than 1 wt%). The XRF elemental composition also presented that the investigated Mn ore sample was indeed an LGMO, which further supported the LIBS

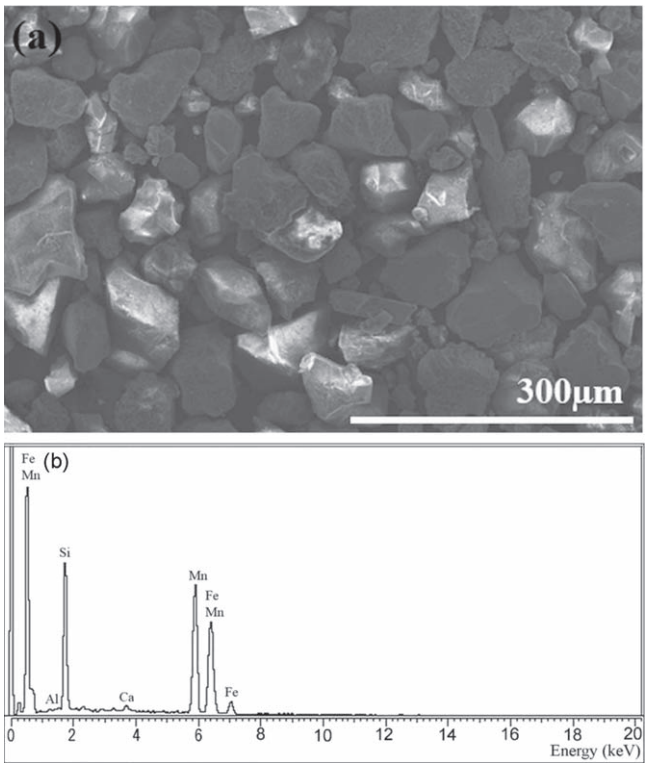

Figure 7. (a) A secondary electron SEM image showing the surface morphology of the Mn ore sample; (b) an SEM-EDS spectrum showing the presence of Mn, Si, Fe, Ca and Al.

spectrochemical analysis. The low Mn content and relatively higher concentration of impurities in LGMO can be attributed to the mineral formation conditions and mechanism. Figure 7(a) shows a secondary electron SEM image of the LGMO sample. The compact pseudo-hexagonal Mn grains are clearly visible in the image. The elemental composition of Mn ore was checked by EDS as well. The observed EDS spectrum shown in figure 7(b) presented Mn (25.05%) and Si (30.48%) as major elements. It was observed that the irregular-shaped grains of light grey contrast were rich in Mn, while Si, Ca, Fe and Al were detected as the other significant impurities. We prepared and examined three Mn samples to study their elemental composition using EDS.

Although the concentration of the detected elements via EDS varied from region to region, the overall composition was almost the same. Unlike the LIBS and XRF results, EDS analysis did not show the presence of some minor/trace elements. The possible reason could be that in the present study, during the EDS analysis, the beam was rastered over a small area compared to the size of the impurity grains to minimize the beam damage. But nevertheless, the obtained EDS spectrum analysis displayed Mn presence in abundance, whereas Si, Ca, Fe and Al were detected as impurities in the investigated LGMO sample, indicating the insignificant difference and excellent agreement within the LIBS and XRF findings. In table 2, we present a comparison of the elemental composition of LGMO obtained using the CF-LIBS method, XRF and EDS. The compositions obtained from these techniques are in good agreement. The LIBS, coupled with the

Table 2. A comparison of the elemental compositions in LGMO determined by different methods (in wt%).

Element	CF-LIBS	XRF	EDS
Si	32.80	31.96	30.48
Mn	26.50	24.17	26.05
Ca	18.90	17.80	17.40
Fe	14.00	15.12	14.87
Al	7.80	7.19	7.85

other analytical techniques, undoubtedly not only assisted but potentially enhanced the understanding of the composition, structure and morphology of the investigated LGMO in the present study.

4. Conclusions

Mn is an important industrial mineral with spread applications. The concentration of Mn in its ore is the parameter used to classify it as high, medium or low grade. It is important to precisely determine the constituent elemental composition, phases and impurities present in Mn to access its suitability for different applications. In the present study, the LGMO samples were investigated qualitatively and quantitatively using LIBS in conjunction with XRD, XRF and SEM-EDS. The analysis of the optical emission spectrum acquired at 1064 nm (fundamental harmonic) of a Nd:YAG laser disclosed the presence of dominant spectral lines for Mn, Si, Ca, Fe and Al, while spectral lines of comparatively lower intensity were observed for Mg, V, Ti, Sr, Ni, Na, Ba and Li. The plasma temperature ($7500\,\mathrm{K} \pm 750\,\mathrm{K}$) and electron number density ($8.18 \pm 0.8 \times 10^{17}\,\mathrm{cm}^{-3}$) were estimated considering the plasma as optically thin and satisfying the LTE condition. XRF analysis of the LGMO sample confirmed the presence of Mn, Si, Ca, Fe and Al as principal elements along with the trace elements, namely Ti, Ni, V, Zn, Sr and Zr. The detection of spessartine, pyrolusite, hausmannite, quartz, pyrochroite, hematite and calcite phases by XRD further confirmed the LIBS and XRF results. The secondary electron SEM image and the corresponding EDS analysis showed that the compact pseudo-hexagonal Mn grains were rich in Mn, and Si, Ca, Fe and Al presented as impurities in large concentrations. The quantitative analyses obtained using the CF-LIBS method, XRF and EDS were observed to be in good agreement. It is further concluded that the XRD, XRF and SEM-EDS methods, coupled with the LIBS, undoubtedly not only assisted but potentially enhanced the understanding of the composition, structure and morphology of the investigated complex nature of LGMO in the present study.

ORCID iDs

Muhammad FAHAD https://orcid.org/0000-0002-0683-0991

References

[1] Sahoo R N, Naik P K and Das S C 2001 *Hydrometallurgy* **62** 157
[2] El Hazek M N, Lasheen T A and Helal A S 2006 *Hydrometallurgy* **84** 187
[3] Hagelstein K 2009 *J. Environ. Manag.* **90** 3736
[4] Gao Y B *et al* 2012 *Metall. Mater. Trans.* B **43** 1465
[5] Mishra P P, Mohapatra B K and Mahanta K 2009 *J. Miner. Mater. Charact. Eng.* **8** 47
[6] Pereira M J, Lima M M F and Lima R M F 2014 *Int. J. Miner. Process.* **131** 26
[7] Mehdilo A, Irannajad M and Hojjati-Rad M R 2013 *Physicochem. Probl. Miner. Process.* **49** 725
[8] Ismail S *et al* 2016 *Period. Mineral.* **85** 277
[9] Ghosh A and Ray H S 1991 *Principles of Extractive Metallurgy* (New Delhi: New Age International (P) Ltd Publishers)
[10] Das S C, Sahoo P K and Rao P K 1982 *Hydrometallurgy* **8** 35
[11] Grimanelis D, Neou-Syngouna P and Vazarlis H 1992 *Hydrometallurgy* **3** 139
[12] Sahoo R N, Naik R N and Das P K 2001 *Hydrometallurgy* **62** 157
[13] Hariprasad D *et al* 2007 *Miner. Eng.* **20** 1293
[14] Su H F *et al* 2008 *Hydrometallurgy* **93** 136
[15] Xie C *et al* 2013 *Chin. J. Geochem.* **32** 222
[16] Sajad A *et al* 2016 *Physicochem. Probl. Miner. Process.* **52** 56
[17] Sajad A *et al* 2018 *J. Miner. Mater. Charact. Eng.* **6** 60
[18] Cremers D A and Radziemski L J 2006 *Handbook of Laser Induced Breakdown Spectroscopy* (England: Wiley)
[19] Hahn D W and Omenetto N 2012 *Appl. Spectrosc.* **66** 347
[20] Galbács G *et al* 2008 *Spectrochim. Acta Part B At. Spectrosc.* **63** 591
[21] Belkov M V *et al* 2009 *Spectrochim. Acta Part B At. Spectrosc.* **64** 899
[22] Gottfried J L *et al* 2009 *Anal. Bioanal. Chem.* **395** 283
[23] Death D L, Cunningham A P and Pollard L J 2009 *Spectrochim. Acta Part B At. Spectrosc.* **64** 1048
[24] Kasem M A, Russo R E and Harith M A 2011 *J. Anal. At. Spectrom.* **26** 1733
[25] Rakovský J *et al* 2014 *Spectrochim. Acta Part B At. Spectrosc.* **101** 269
[26] Lennard C, El-Deftar M M and Robertson J 2015 *Forensic Sci. Int.* **254** 68
[27] Yongcheng J *et al* 2017 *J. Appl. Spectrosc.* **84** 103
[28] An L, Saho Q F and Liu R B 2017 *Chin. J. Opt.* **10** 426 (in Chinese)
[29] Harmon R S *et al* 2018 *J. Archaeol. Sci.* **98** 112
[30] Cuñat J *et al* 2005 *J. Anal. At. Spectrom.* **20** 295
[31] Harmon R S *et al* 2006 *Anal. Bioanal. Chem.* **385** 1140
[32] Harmon R S *et al* 2009 *Appl. Geochem.* **24** 1125
[33] Harmon R S, Russo R E and Hark R R 2013 *Spectrochim. Acta Part B At. Spectrosc.* **87** 11
[34] Harmon R S *et al* 2017 *Geostand. Geoanal. Res.* **41** 563
[35] Hark R R *et al* 2012 *Spectrochim. Acta Part B At. Spectrosc.* **74–75** 131
[36] Qiao S J *et al* 2015 *Appl. Spectrosc. Rev.* **50** 1
[37] Jantzi S C *et al* 2016 *Spectrochim. Acta Part B At. Spectrosc.* **115** 52
[38] Senesi G S 2017 *Int. J. Earth Environ. Sci.* **2** 146
[39] Abrar M *et al 2018 Laser Phys.* **28** 056002
[40] Fahad M and Abrar M 2018 *Laser Phys.* **28** 085701
[41] Fahad M *et al* 2018 *Laser Phys.* **28** 125701
[42] Kramida A, Ralchenko Y, Reader J and NIST ASD Team 2019 National Institute of Standards and Technology http://physics.nist.gov/asd
[43] Griem H R 2005 *Principles of Plasma Spectroscopy* (Cambridge: Cambridge University Press)

[44] Cristoforetti G *et al* 2010 *Spectrochim. Acta Part B At. Spectrosc.* **65** 86
[45] Griem H R 1974 *Spectral Line Broadening by Plasma* (New York: London Academic Press, Inc.)
[46] McWhirter R W P 1965 *Spectral intensities Plasma Diagnostic Techniques* ed R H Huddleston and S L Leonard (New York: Academic)
[47] Ahmed N *et al* 2017 *Laser Part. Beams* **35** 1
[48] Farooq Z *et al* 2018 *Phys. Plasmas* **25** 093106
[49] Miziolek A W, Palleschi V and Schechter I 2006 *Laser Induced Breakdown Spectroscopy (LIBS) Fundamentals and Applications* (New York: Cambridge University Press)
[50] Unnikrishnan V K *et al* 2012 *Pramana* **79** 299